



Magnetic resonance imaging of the mouse visual pathway for *in vivo* studies of degeneration and regeneration in the CNS

Ronny Haenold ^{a,*}, Karl-Heinz Herrmann ^b, Silvio Schmidt ^c, Jürgen R. Reichenbach ^b,
Karl-Friedrich Schmidt ^d, Siegrid Löwel ^{d,1}, Otto W. Witte ^c, Falk Weih ^a, Alexandra Kretz ^c

^a Leibniz-Institute for Age Research, Fritz-Lipmann-Institute (FLI), Beutenbergstrasse 11, 07745 Jena, Germany

^b Friedrich-Schiller-University of Jena Medical School, Institute of Diagnostic and Interventional Radiology I, Medical Physics Group, Philosophenweg 3, 07743 Jena, Germany

^c Friedrich-Schiller-University of Jena Medical School, Department of Neurology, Erlanger Allee 101, 07747 Jena, Germany

^d Friedrich-Schiller-University of Jena, Institute of General Zoology and Animal Physiology, Erbertstrasse 1, 07743 Jena, Germany

ARTICLE INFO

Article history:

Received 11 March 2011

Revised 24 June 2011

Accepted 22 July 2011

Available online 30 July 2011

Keywords:

Mouse retino-tectal projection

Manganese-enhanced MRI

Neuronal regeneration

Neuronal degeneration

NF-κB

3 T clinical scanner

ABSTRACT

Traditionally, depiction of isolated CNS fiber tracts is achieved by histological post mortem studies. As a tracer-dependent strategy, the calcium analog manganese has proved valuable for *in vivo* imaging of CNS trajectories, particularly in rats. However, adequate protocols in mice are still rare. To take advantage of the numerous genetic mouse mutants that are available to study axonal de- and regeneration processes, a MnCl₂-based protocol for high-resolution contrast-enhanced MRI (MEMRI) of the visual pathway in mice acquired on a widely used clinical 3 Tesla scanner was established. Intravitreal application of MnCl₂ significantly enhanced T1-weighted contrast and signal intensity along the retino-petal projection enabling its reconstruction in a 3D mode from a maximum intensity projection (MIP) calculated dataset. In response to crush injury of the optic nerve, axonal transport of MnCl₂ was diminished and completely blocked proximal and distal to the lesion site, respectively. Conditions of Wallerian degeneration after acute optic nerve injury accelerated Mn²⁺-enhanced signal fading in axotomized projection areas between 12 and 24 h post-injury. In long-term regeneration studies 12 months after optic nerve injury, the MRI protocol proved highly sensitive and discriminated animals with rare spontaneous axonal regrowth from non-regenerating specimens. Also, structural MRI aspects shared high correlation with histological results in identical animals. Moreover, in a model of chronic neurodegeneration in p50/NF-κB-deficient mice, MnCl₂-based neuron-axonal tracing supported by heat map imaging indicated neuropathy of the visual pathway due to atrophy of optic nerve fiber projections. Toxic effects of MnCl₂ at MRI contrast-relevant dosages in repetitive administration protocols were ruled out by histological and optometric examinations. At higher dosages, photoreceptors, not retinal ganglion cells, turned out as most susceptible to the well-known toxicity of MnCl₂. Our data accentuate *in vivo* MEMRI of the murine visual system as a highly specific and sensitive strategy to uncover axonal degeneration and restoration processes, even in a functional latent state. We expect MEMRI to be promising for future applications in longitudinal studies on development, aging, or regeneration of CNS projections in mouse models mimicking human CNS pathologies.

© 2011 Elsevier Inc. All rights reserved.

Introduction

Axonal pathologies of CNS fiber projections, e.g. after acute spinal cord injury, stroke, or in neurodegenerative diseases, indicate special diagnostic means to address structural alterations at incipency, and to monitor treatment efficacy or to predict disease progression. Apart from diffusion tensor (DT)-MRI and MR-spectroscopy, which are commonly

reserved to peculiar indications, non-invasive MRI sequences are standard in clinical brain imaging, for analysis of local CNS circuits, and volume calculations. However, the concomitantly applied contrasting agent Gadolinium (Gd)-DTPA accumulates only at site of disrupted blood brain barrier (BBB), and often neglects non-inflammatory pathology of single fiber projections. In experimental *in vivo* paradigms, e.g. in animal models, tracer substances such as biotinylated dextran, Fluorogold, Dil, or horseradish peroxidase can be directly applied to the neuronal soma or to synaptic terminals to label centrifugal or centripetal fiber projections. Neurotropic reporter gene coupled Herpes simplex virus constructs trace trans-synaptic projections when locally administered to the brain region of interest. Such chemical tracing processes always require the sacrifice of animals for subsequent histological examinations as well as time intense software reconstructions of serial sections. An elegant technique for *in vivo* fiber tract visualization in

Abbreviations: CNR, contrast-to-noise-ratio; SNR, signal-to-noise-ratio; *ivit*, intravitreal injection; MEMRI, manganese-enhanced MRI.

* Corresponding author. Fax: +49 3641 656335.

E-mail address: rhaenold@fli-leibniz.de (R. Haenold).

¹ Present address: Georg-August-University, Bernstein Focus Neurotechnology and Johann-Friedrich-Blumenbach Institute for Zoology und Anthropology, Berliner Strasse 28, 37073 Göttingen, Germany.

several species including mice, rats and non-human primates represents the use of Mn²⁺-enhanced MRI (MEMRI) as pioneered by Watanabe et al. (2001, 2004a, b), Pautler (2004), Pautler and Koretsky (2002) and Pautler et al. (1998, 2003). Meanwhile, their original work has been extended and comparative DTI studies and MEMRI features on acutely injured and chronically degenerating axonal CNS projections are available (Kim et al., 2011; Thuen et al., 2008, 2009). Neuroanatomically, sensory CNS tracts such as the olfactory, visual and auditory projection have become focus of MEMRI (Pautler and Koretsky, 2002; Watanabe et al., 2001, 2008). However, it also unmasked structural alterations in the prefrontal to mesocortical reward-modulating circuitry in dopamine transporter *knockout* mice that had remained underestimated even by voxel-wise statistical MRI analysis (Zhang et al., 2010). Further genetically modified mouse mutants served to characterize physiological suppositions and pathological impairments of axonal Mn²⁺ transport. Likewise, altered transport velocities were exemplified in triple transgenic mice mimicking Alzheimer tauopathy (Kim et al., 2011). Bearer et al. (2007) investigated the role of neuronal activity on trans-synaptic Mn²⁺ propagation and its dependence on kinesin-mediated axonal transport. The activity dependence of Mn²⁺ propagation was used for fMRI-like MEMRI studies on *in vivo* mapping of the auditory pathway in which the tonotopic representation of the inferior colliculi under frequency modulated acoustic stimulation was presented in a highly sophisticated manner (Yu et al., 2005). Similar studies could recapitulate the retinotopic structural organization of the superior colliculi (Chan et al., 2011). Most importantly, the chelated FDA-approved Mn²⁺ derivative manganese dipyridoxyl diphosphate (MnDPDP, Teslascan) is already under clinical application, e.g. for increasing diagnostic sensitivity of MRI on liver and pancreas, and a first experimental study on intravenous application of Teslascan at clinically relevant doses in SD rats and for imaging of the visual pathway are already available (Olsen et al., 2008, Tofts et al., 2010).

Biophysically, paramagnetic Mn²⁺ and Gd-DTPA augment magnetic resonance contrast mainly by shortening T1 spin-lattice relaxation time (Howles et al., 2010; Mendonca-Dias et al., 1983). As a calcium (Ca²⁺) analog, Mn²⁺ is incorporated in neurons by voltage-gated calcium channels and becomes actively transported along intact microtubules of the axonal cytoskeleton, whereas passive diffusion into the tissue is negligible. Its propagation is interrupted both mechanically and toxically, e.g. in injured axonal trajectories (Thuen et al., 2005) and upon cholchicine treatment (Tillet et al., 1993). It accumulates as a function of membrane integrity and cell activation, and is retained intracellularly in vesicles for longer time intervals. MEMRI of distinctive CNS structures has been shown to be feasible in rodents following its systemic intravenous (Boretius et al., 2008), intraperitoneal, or subcutaneous (Watanabe et al., 2002, 2004a; Yu et al., 2005) and local, e.g. stereotaxic (Pautler et al., 1998; Watanabe et al., 2004b; Zhang et al., 2010) or aerosolized (Pautler and Koretsky, 2002) administration.

Here, we introduce a novel MEMRI protocol to dissect axonal disorders in mice using T1-weighted sequences. In contrast to recent studies on mice performed with 7.0 up to 11.7 T high resolution magnetic resonance machines (Lindsey et al., 2007; Zhang et al., 2010), images were acquired on a conventional clinical 3 T scanner, thus providing technical accessibility to a much broader audience in neuroscience research. MnCl₂ solutions were applied intravitreally (*ivit*), and time- and concentration-dependent alterations of T1-weighted contrast and signal intensities were monitored along retino-recipient projections in naïve animals. Furthermore, the impact of acute CNS fiber injury on MnCl₂ propagation was investigated following optic nerve (ON) crush injury. In rodents, mechanical crush of the ON that causes breakage of axonal cylinders (axonotmesis) has become an established experimental paradigm to study traumatic responses of CNS fiber projections (Benowitz and Yin, 2008). In this paradigm, the sensitivity of MEMRI to identify axonal regrowth was correlated with classical histological procedures 12 months after injury.

Further, MEMRI was addressed on instances of pathologic brain senescence. A variety of neurodegenerative diseases involve apoptotic loss of neuronal cell bodies as well as atrophy and degradation of axonal trajectories such as stroke, Alzheimer's dementia, amyotrophic lateral sclerosis and glaucoma (Ferri et al., 2003; Libby et al., 2005; Stokin et al., 2005). The transcription factor NF-κB controls neuronal maintenance and mice with a deletion of the p50 subunit of NF-κB (p50^{KO/KO}) have been used as an experimental model for age-dependent axonal degeneration in the visual system (Takahashi et al., 2007). To further test MEMRI in the detection of projection-specific fiber atrophy we used NF-κB p50 mutant mice as a model for chronic neuronal and axonal degeneration and compared their visual projection with other pigmented and non-pigmented mouse strains.

To define overall feasibility of MnCl₂ application in mice we performed susceptibility and toxicity studies and functional visual tests after both single as well as repetitive tracer applications in individual animals and demonstrate cell type-specific vulnerabilities towards MnCl₂ exposure.

In summary, our study extends the already available studies on MEMRI by providing detailed biophysical and pharmacological information on optimal dosages, transport kinetics and toxicity of MnCl₂ especially for mice. Toxicity studies were confirmed by histological *post mortem* and functional *in vivo* investigations. As a technological advantage, we introduce a MRI protocol making high resolution imaging feasible in small rodents even with a low field 3 T scanner. This protocol proved useful in mouse models of neuroregeneration and Waller degeneration to detect regrowth and atrophy of CNS axons. With respect to the FDA-approved manganese derivative Mangafodipir, we suggest this MEMRI technique to be highly promising for further single and serial *in vivo* applications, e.g. to serve as a tool for early diagnostics and therapeutic approval strategies in humans.

Methods

Animals and injury models

For pharmacokinetic and injury studies inbred C57BL/6 (B6) mice of mixed gender and an average age of 15 weeks were used. To investigate mouse strain specific differences, additional studies were performed using NMRI outbred and Balb/c inbred mice. As a genetic model for chronic neuronal and axonal degeneration (Takahashi et al., 2007), mice lacking the p50 subunit of NF-κB on a B6 background at 10 months of age were used (Sha et al., 1995). Animals were kept under controlled conditions in a specific pathogen free environment.

Acute crush injury of the optic nerve (ON) was performed immediately before *ivit* MnCl₂ application. Frequently, ON crush in rodents is performed by a micro-operative intervention, where scalp and superior palpebrae are incised and the dural nerve sheath is exposed to reach the ON for crushing with a microforceps (Berry et al., 1999; Thuen et al., 2005). Here, we applied a simplified procedure and squeezed the mouse ON between the tilted branches of a small forceps 1.5 mm directly behind the posterior eye pole for 10 s without surgical exposure. Injured mice were investigated by MRI 12 and 24 h after acute ON injury (ONI) and 12 months thereafter to study long-term axon regeneration.

For all ocular interventions, mice were deeply anesthetized by weight-adapted *i.p.* injection of a sterile 5% chloral hydrate solution (420–450 mg/kg body weight in sterile PBS; Sigma Aldrich, Germany). For additional topical anesthesia, liquid conjucain (0.4%; Dr. Mann Pharma, Germany) was applied to the cornea prior to eye puncture.

For MRI, anesthesia was induced by placing the animal into a glass cylinder with inflow of a 2%/100% isoflurane/oxygen gas compound. During MRI, anesthesia was afforded by continuous insufflation of a 1.75%/100% isoflurane/oxygen gas compound via an evaporator (Vapor 19.3; Dräger Werk AG Lübeck, Germany) connected to the mouse head holder (custom made, Suppl. Fig. 1) by an integrated tube. To protect

body temperature, animals were covered with tissue throughout the MRI. Post-MRI, animals were supplied with pure oxygen and vital parameters were monitored for 2 h after inhalation anesthesia.

All animal interventions were performed in accordance to the European Convention for Animal Care and Use of Laboratory Animals and approved by the local ethic committee.

Tracer applications

Intravitreal tracer application to the eye (*ivit*; uni- or bilaterally) of fully anesthetized mice was facilitated by the use of a sterile 5 μ l Hamilton syringe connected to a 34 G needle. Atraumatic puncture of the eye bulb was reproducibly performed in the infero-temporal circumference (at 5 and 7 o'clock for the left and right eye, respectively) approximately 1 mm distal of the limbus, thereby sparing scleral vessels. To monitor needle placement as well as liquid inoculation and eye turgor, microinjections were accomplished under a binocular microscope. The inserted needle was kept for about 1 min and slowly withdrawn to minimize substance leakage from the injection site. To prevent ocular infections and drying of the eye, ofloxacin containing eye drops and ointment were once applied.

For MRI tracing studies, 2 μ l of a sterile $MnCl_2/H_2O$ solution (see below) were applied to the eyes. For fluorescence microscopic analysis of fiber regeneration and sprouting, 2 μ l of Cy3-conjugated cholera toxin B subunit (CTX-594; 1 μ g/ μ l; C-22842, Molecular Probes, U.S.A.) was *ivit* injected 2–3 days prior to ONI to allow its propagation along ON axons. Complete disappearance of the Cy3 conjugate during the following weeks and months indicated total fiber degeneration. Complementary FITC-labeled cholera toxin B subunit (2 μ l of CTX-488; 1 μ g/ μ l; C-22841, Molecular Probes, U.S.A.) was then applied to the retina 2–3 days prior to final histological dissection to identify newly generated axons. Although small injection volumes may transiently impair electrical RGC activity (Bearer et al., 2007), functional measurements on visual acuity and contrast sensitivity (see below) 2 and 14 days after intraocular injection of 2 μ l saline excluded noxious effects on vision by such volume stress (Table 2).

$MnCl_2$ protocols

To study concentration-dependent contrasting effects, animals were *ivit* injected with single $MnCl_2$ doses (Sigma Aldrich, Germany) of 0.15, 1.5, 15, 150, and 1500 nmol 24 h before MRI. Water-injected animals were taken to determine tracer specific enhancement of SNR/CNR in according brain areas. For kinetic studies, animals were injected with a single dose of 15 nmol $MnCl_2$ and MRI protocols were applied 6, 12, 24, 48, 72, and 120 h thereafter. For acute and chronic injury models a single application of 15 nmol $MnCl_2$ was performed which is less than a third of the concentration used in other murine studies (Bearer et al., 2007). For repetitive injections, 6 applications of each 15 nmol were exerted within a 2 months time period. In the

Table 1

Summary on animal numbers used for experimental procedures.

Experimental procedure	Group numbers N	
	Treatment	Control
Dosage study (Fig. 1)	52	6
Kinetic study (Fig. 1)	32	9
Mouse strain study (Fig. 2)	8	–
Optic nerve injury study (Fig. 3)	9	9
Optic nerve degeneration study (Fig. 3)	4	4
Optic nerve regeneration study (Fig. 4)	8	8
Degeneration in $p50^{KO/KO}$ study (Fig. 5)	8	9
Optometry for dosages (Fig. 6)	48	12
Optometry for serial injections (Fig. 6)	24	12
Toxicity study (Fig. 7)	17	6

Table 2

Impact of intraocular volume stress on visual acuity as assessed by virtual-reality optometer in mice. Animals with an intravitreal volume of 2 μ l PBS displayed physiological visual acuity with a mean value of 0.38 p/m 0.0001 cyc/deg, which was indistinguishable from uninjected controls 2 and 14 days thereafter ($P=0.9$). dpi, days post injection. SE, standard error.

Eye	Control	2 dpi	14 dpi
1	0.375	0.381	0.381
2	0.375	0.381	0.381
3	0.381	0.372	0.383
4	0.381	0.372	0.383
5	0.383	0.386	0.375
6	0.383	0.386	0.375
7	0.372	0.381	0.381
8	0.372	0.369	0.381
9	0.386	0.381	0.375
10	0.386	0.381	0.375
11	0.378	0.378	0.381
12	0.378	0.378	0.381
Average	0.38	0.38	0.38
SE	0.001	0.002	0.001
P		0.9	0.9

acute injury model, $MnCl_2$ was applied either immediately after crush or, in a limited additional series, 12 h prior to the crush.

MRI protocol

MRI was performed using a clinical 3 Tesla scanner (Siemens, Germany) and a rat head Litz coil (Doty, Inc., U.S.A.). Images were acquired by coronal and transversal measurement direction. The employed 3D FLASH sequence (VIBE 3D) acquired data with the following parameters: isotropic spatial resolution of (0.2 mm)³, matrix 256 \times 240 \times 78, echo time $T_E=6.51$ ms, repetition time $T_R=16$ ms, band width = 444 Hz/px, flip angle $\alpha=22^\circ$. Applying 2 averages and 3 repetitions, a total T_A (acquisition time) of approximately 30–35 min was achieved. Details of the MRI protocol run are also found in Table 3.

MRI data analysis

Images were processed using the software *Syngo Fast Viewer* (Siemens, Germany) and standard commercial software. Two-dimensional planar MRI recordings and multiplanar reconstructions (MPR) calculated from the original 3D MRI data set were depicted as horizontal and coronal images, respectively. A mouse brain atlas (Franklin and Paxinos, 1997) facilitated neuro-anatomic orientation. Contrast-to-noise ratio (mean CNR) was calculated by subtracting the tissue background signal from the average MRI signal intensity (mean signal) within a defined region-of-interest (ROI), divided by the standard deviation of the noise. In some cases, additional to the mean

Table 3

Summary of MRI parameters using a clinical 3 T whole-body scanner (Magnetom TIM Trio, Siemens Medical Solutions, Erlangen, Germany).

Parameter	T_1 -weighted GRE
Isotr. resol. [mm]	0.2
Matrix	256 \times 240 \times 78
FoV [mm]	54 \times 53 \times 14
NEX ^b	6
bandwidth [Hz/px]	444
α [°]	22
PF slice	8/8
PF phase	8/8
TF	–
T_R [ms]	16
T_E [ms]	6.51
T_A [min]	30

CNR, maximum CNR values were determined based on the strongest contrast-enhanced MRI signal. This parameter indicates the peak Mn^{2+} accumulation within the selected ROI and, therefore, is independent of gradual or inhomogeneous tracer distribution. ROI areas were selected according to resolved anatomical structures. For each sample, three subsequent images were analyzed and the average CNR value was calculated. In bilaterally injected animals, hemispheres were analyzed independently. Animated 3D reconstructions of the retino-tectal projection were created from maximum intensity projections (MIP) using an angiography post processing software module (Siemens, Germany). Thereby, for each pixel of a specific projection, the maximal CNR is calculated from the stack and given in the output picture.

Histology and immunocytochemistry

Mice were *ivit* injected with a single dose of 0, 15, 50, and 100 nmol $MnCl_2$ and eyes were dissected 14 days later. The tissue was fixed in 4% paraformaldehyde/PBS (pH 7.4) and 16 μm equatorially cut frozen sections were prepared. For histomorphological analysis, specimens were stained with H&E. Immunofluorescent labeling of photoreceptor and ganglion cell layers was performed using antibodies against recoverin (1:500, AB5585, polyclonal, Chemicon, U.S.A.; 203F polyclonal, kind gift from J.F. McGinnis, Oklahoma) and the monoclonal RGC detecting beta-III tubulin marker TUJ-1 (1:250; MMS-435P, Covance, U.S.A.), respectively. Cy3- or Alexa-conjugates of adequate secondary antibodies were used to visualize primary antibody binding. Size acquisition of the photoreceptor layer was performed by measuring the extent of recoverin-positive nuclear and disk areas on transversal retinal sections. RGC densities were assessed on flat mounted retinal preparations after immunocytochemical staining with the TUJ-1 antibody using double-blind protocols (Isenmann et al., 2004). RGC numbers were quantified from pictures taken at a fluorescence microscope (ApoTome; Zeiss, Germany) at 3–4/6 radial eccentricities from the optic disk.

The ON of mice which had obtained unilateral crush injury and dual ipsilateral anterograde CTX-injections were isolated 12 months after injury and 3 days after second CTX-injection. Longitudinal 16 μm cryosections were cut from the *lamina cribrosa* up to 0.5–1 cm along the axis of the ON comprising the suggested injury and scar region. Sections were fixed in 4% paraformaldehyde/PBS (pH 7.4) and incubated with monoclonal SMI-31 antibody against phosphorylated neurofilaments (1:250–1:500; SMI-31R, Covance, U.S.A.) followed by incubation with a secondary AMCA antibody (1:50; Dianova, Jackson Immuno Research Laboratories, U.S.A.) for 1 h.

Optometric test

Visual acuity and contrast sensitivity were assessed 14 days after *ivit* $MnCl_2$ injection using a virtual-reality optomotor system based on the evocation of the optokinetic reflex (Lehmann and Löwel, 2008; Prusky et al., 2004). Briefly, freely moving animals were exposed to moving sine wave gratings of various spatial frequencies and contrasts. Reflexive tracking of the gratings was analyzed by monitoring head movements up to detection thresholds (Prusky et al., 2004). For each group, at least 5 animals were assessed.

Statistical analysis

Statistical analyses were performed using Student's *t*-test, followed by post hoc ANOVA. Data are presented as mean \pm standard error. For manganese dose response and time kinetic studies, 58 and 41 retino-tectal hemiprojections were analyzed in repetitive sessions, respectively. For each other experiment, 3–7 animals, i.e. 6–14 visual hemiprojections were investigated. If not otherwise indicated, N numbers given in the text represent the number of individually

analyzed eyes and visual hemiprojections. An overview on the number for each experimental procedure is given in Table 1.

Results

MRI protocol for MEMRI in mice with a 3 T clinical scanner

Accounting for the limited field strength of our clinical 3 T scanner, we established a novel MEMRI protocol with modulated parameters. To improve SNR we repeated each scan twice with internal averaging, and repeated this 10 min examination 3 times for later averaging of the magnitude images. This allowed for an acquisition time of 5 min for one single scan of the entire volume. The 35 min total scan time included 5 min localizer and pre-scans and 30 min for the actual MEMRI imaging.

Since a 2D approach was not feasible due to the limited gradient strength, which allowed only a minimal slice thickness of approximately 1 mm, we preferred a 3D acquisition mode in which the whole excited volume contributes to the signal. Commonly, long TE/TR of 12 ms/250 ms of 2D T1 weighted spin-echo sequences are necessary to accommodate to a 180° refocusing pulse and to allow multi-slice mode acquisition. An excitation flip angle of 60° to 90° is then required to achieve the T1 weighted contrast. In our case, applying the 3D acquisition mode, TE/TR were adapted to 6.51/16 ms at a flip angle of 22° accounting for the difference that we used a 3D spoiled gradient-echo sequence (aka GRE, FLASH) instead of the common spin-echo sequence. TE and TR were set to minimum to minimize total TA. Although a total acquisition time of 30 min is inadequate to follow fast dynamic processes, it still allows to assess Mn^{2+} transport progression over several hours as outlined in our kinetic study (Fig. 1C).

Dosage for $MnCl_2$ -enhanced MRI of the mouse visual system

The neuroanatomical structures of the rodent visual system comprise extra-cerebral retina and optic nerve (ON), whose fibers decussate intra-cranially at the optic chiasm to form the optic tract, and its major cerebral projection areas, the thalamic *lateral geniculate nucleus* (LGN) and midbrain *superior colliculus* (SC) (Dräger and Olsen, 1980; Hayhow et al., 1962). These structures showed a clear MRI signal enhancement in transversal planar 2D slices within a well-defined $MnCl_2$ dosage range of 15–150 nmol (Fig. 1A, sharp arrows). To quantify the apparent contrast enhancement, the contrast-to-noise ratio (CNR) for the ON, LGN, and SC were analyzed. No or only minor changes in CNR were observed after *ivit* injection of 0.15 (N=6) and 1.5 nmol (N=8) $MnCl_2$ compared to water-injected controls (Figs. 1A and B; N=58). At 15 nmol $MnCl_2$ (N=8), CNR strongly increased to 53.2 ± 1.5 (2.5-fold) in the ON, to 18.8 ± 1.2 (8-fold) in the retino-recipient lateral and ventral LGN, and to 17.9 ± 0.8 (45-fold) in the superficial layer of the SC (Fig. 1B). In the maximum intensity projection (MIP) mode, the composed projection of the enhanced structures at the periphery, including eyes and optic nerves (ONs), and centrally the optic tracts, LGN and SC became 3-dimensionally visible. Fig. 2A exemplifies high-resolution top (a) and lateral (b) views of the mouse brain after bilateral injection of 15 nmol $MnCl_2$. An animated, 3-dimensional presentation of the *in situ* retino-tectal 3D architecture is available online (suppl. File 1). Noticeably, we did not find evidence for signal enhancement above background levels along the geniculo-striate pathway including Meyer's loop and Baum's loop, the V4 recipient field or in V1 of the primary visual cortex as reported for rats (Thuen et al., 2005) and suggested for mice (Lindsey et al., 2007). Increasing the dosage of $MnCl_2$ to 50 or 150 nmol (N=12) did not further enhance MRI signal intensity and at 1500 nmol (N=6) CNR was reduced and even abolished along the ON and in the midthalamic brain regions (Figs. 1A, broad arrows, and B). Macroscopically, eyes injected with 1500 nmol $MnCl_2$ displayed severe dystrophy and intraocular pathology including retinal atrophy and bleedings into retina and vitreous body and MRI measurements were disturbed by contrast artifacts. Thus, as previously described for rats (Thuen et al.,

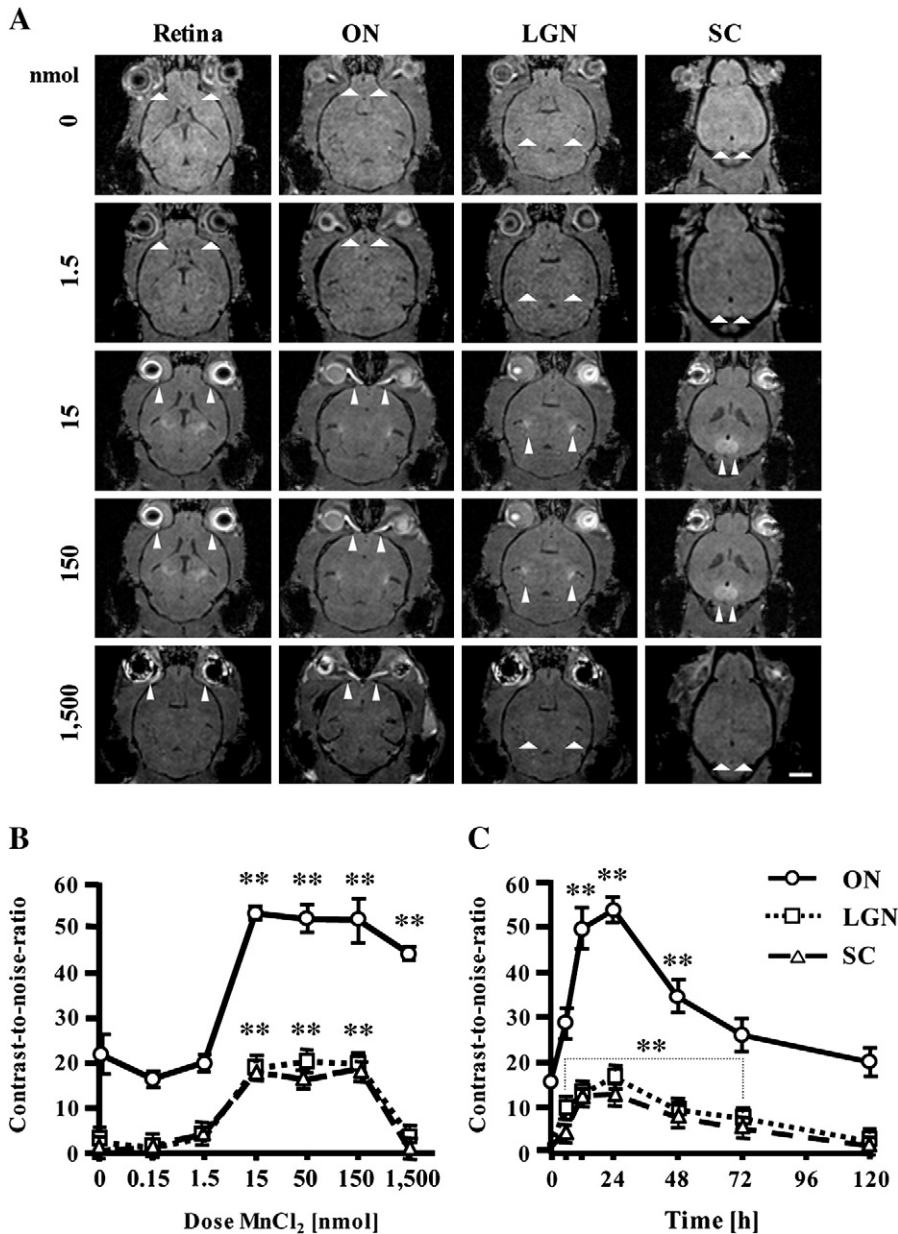


Fig. 1. Dose and time response of Mn²⁺-enhanced MR-imaging (MEMRI) of the mouse retino-tectal projection. (A) Transversal planar 2D images and (B) graphical representation of dosage-dependent signal enhancement in retina, optic nerve (ON), lateral geniculate nucleus (LGN) and superior colliculus (SC) following *ivit* injection of MnCl₂. (C) Time kinetic of signal enhancement along the retino-tectal projection measured with 15 nmol MnCl₂. Scale: 2 mm. ***P*<0.01.

2008), excessive MnCl₂ administration to mouse retina resulted in a block of axonal MnCl₂ transport along the afferent retino-tectal projection. Taken together, *ivit* injection at a dosage of 15 nmol MnCl₂ proved to be adequate and sufficient for maximum contrast-enhanced MRI of the mouse visual projection. Similar signal enhancements as in 15 nmol MnCl₂-treated B6 mice were calculated for outbred NMRI and inbred Balb/c mice (Fig. 2B and data not shown). Heat map imaging of coronal and horizontal section planes after unilateral MnCl₂ injection in NMRI mice is shown in Fig. 2B. Generally, the achieved signal enhancement in mice described in this study required a 10- to 20-fold lower MnCl₂ dosage than that previously reported for rats (Thuen et al., 2008).

Kinetics of Mn²⁺-enhanced MRI in the mouse visual system

In rats, anterograde MnCl₂ transport is known to peak at 24 h in the ON and after 48 h in the SC (Thuen et al., 2008). Given the smaller

anatomical dimensions of the mouse brain and a putatively faster axonal transport rate (Pautler et al., 1998), we aimed to optimize the time window for optimal tracing of murine retino-tectal structures. Therefore, mice with a bilateral single injection of 15 nmol MnCl₂ were repeatedly examined by MRI to monitor response of signal enhancement over time. Non-injected animals served as controls (0 h) and, according to anatomical structures, CNR in ON, LGN, and SC was assessed. CNR of all areas investigated was strongly enhanced 12 h after *ivit* injection, peaked at 24 h (CNR, ON: 53.7 ± 2.7; LGN: 16.8 ± 1.7; SC: 13.0 ± 2.2; *P*<0.05, N=6) and continuously decreased back to baseline values during a total time of 120 h post-injection (Fig. 1C; N=41). Thus, the optimal time window for maximum contrast in MEMRI measurements of the mouse visual system was 12–24 h after *ivit* Mn²⁺ application, which represents half of the enhancement time needed in rats (Thuen et al., 2005). Analysis of maximum CNR values calculated from the spot with the highest signal intensity instead of the averaged signal intensity in each ROI area gave

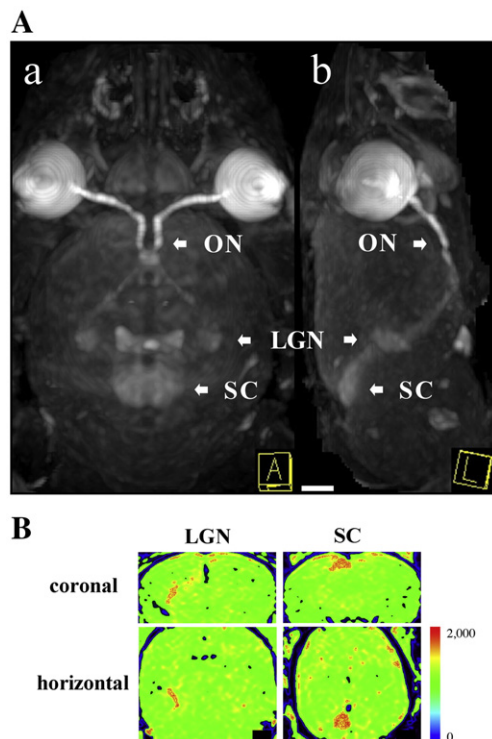


Fig. 2. MEMRI of the retino-tectal projection in different mouse strains. (A) Top (a) and lateral (b) view on a multiplanar 3D MIP reconstruction of the bilaterally enhanced visual projection in the B6 inbred mouse strain. ON, LGN, and SC are indicated by arrows. (B) Heat-color presentation of topical signal enhancement (red) in the LGN and SC after unilateral *ivit* injection of 15 nmol MnCl_2 in the NMRI outbred mouse strain. Maps were analyzed in the coronal and horizontal plane. In the color-encoded images, hot colors represent higher MRI signals than cold colors. Scale: 1 mm.

a similar curve shape as for the mean CNR with higher peak values (CNR, LGN: 24.8 ± 2.2 ; SC: 23.0 ± 2.0 at 24 h). Interestingly, these graphs revealed a steeper incline, and the signal for the ON already peaked at 12 h (72.9 ± 1.4), suggesting a higher sensitivity of this algorithm for the detection of early changes in tissue contrasting.

Signal intensity in all considered regions was increased at least 6 h after injection. With an approximated length of the retino-tectal projection in the mouse of 2 cm, this time-response is in line with a proposed fast axonal transport rate of 2–6 mm/h for manganese ions (Pautler et al., 1998; Thuen et al., 2005). Accounting for the longer distances in rats, transport velocities in mice and rats seem highly comparable (Thuen et al., 2005).

Acute injury model

Crush injury of the ON causes immediate interruption of electrical transmission in the broken axonal fascicles followed by progressive Wallerian degeneration of the proximal and distal nerve stump. As compared to the peripheral nervous system, its progression occurs much slower. Accordingly, ONI caused an immediate and complete loss of visual function, as determined by an optometric assay 3 h post-injury (Fig. 3A; $N=9$). In addition to this functional breakdown, transport of MnCl_2 along the axonal cytoskeleton was completely blocked after ONI as visualized by an abrupt and complete loss of MnCl_2 -enhanced signal beyond the injury site (Fig. 3B; CNR=0; $P<0.01$, $N=9$). Thus, *in vivo* MRI was successfully used to confirm *in toto* lesion of the RGC axon projection by crush injury. Maximum intensity projections (MIP) acquired from images with an isotropic resolution of $(0.2 \text{ mm})^3$ enabled the identification of the lesion site in the living mouse 0.8 mm behind the *lamina cribrosa* (Fig. 3B). Furthermore, modifying the sequence of MnCl_2 application enabled us to observe over time the degeneration process of disconnected

axon segments distal to the lesion site. For such experiments, we first *ivit* injected the MnCl_2 solution, allowing continuous enhancement of the retino-tectal projection. The Mn^{2+} -filled ON was then crushed 12 h later and MRI was performed with an additional delay of 12 and 24 h to visualize the degeneration process (Fig. 3C, Table 4). Unexpectedly, tracer enhancement was significantly reduced along the entire injured projection, displaying a signal intensity reduction by $38.8 \pm 9.6\%$ ($P<0.01$, $N=4$) in the LGN and $29.8 \pm 11.3\%$ in the SC ($P<0.05$, $N=4$) already 12 h after the crush. Longitudinal investigation of 4 individual animals 24 h after ONI confirmed a considerable signal reduction in proximal and distal parts of the severed ON and an almost complete loss of signal in the SC (Fig. 3D, Table 4). Thus, tracer fading appeared most prominently in the very distal parts of the visual projection where Wallerian degeneration is supposed to initiate. Impaired tracer enrichment by insufficient tracer propagation 12 h after application was excluded since the unimpaired contralateral site showed CNR ratios of well-defined maximum range. According to our kinetic studies, saturation of Mn^{2+} uptake is achieved between 12 and 24 h after tracer application with non-significant further CNR augmentation between 12 and 24 h (Fig. 1C). Thus, the time window of 12 h chosen in this experiment is adequate to achieve maximum tracing values.

Post injury axonal regeneration

Even unstimulated severed RGC are capable of limited spontaneous fiber regeneration (Kretz et al., 2005). Here, we used MEMRI as an *in vivo* marker to identify whether there is long-term regeneration 12 months after crush injury of the ON. While MnCl_2 transport arrested 0.8 mm behind the *lamina cribrosa* immediately after crush (Fig. 3B, $N=9$), the tracer was again propagated up to 1.4 mm within the ON sheath 12 months after injury (Figs. 4A–E, $N=8$) suggesting that – at least some – regenerating fibers had elongated through the injury site. To confirm this, animals from the MRI measurements were anterogradely injected with CTX-488 conjugates (green) and analyzed by immunohistochemistry 3 days later (see Methods). Histological evaluation of longitudinal cryosections through the ON revealed retrograde Wallerian degeneration of the retracted proximal axon stump as confirmed by complete loss of the CTX-594 fluorochrome (red) injected already 12 months before and prior to crush injury. Furthermore, CTX-488 incorporation in SMI-31 positive, CTX-594 negative filigree structures indicated few newly generated axons, which had elaborated up to 1.2 mm behind the *lamina cribrosa* (Fig. 4F). Thus, MRI based regeneration analysis highly correlated with standard histological analysis.

Chronic degeneration model

As a model for chronic neurodegeneration, we investigated the potential of *in vivo* MEMRI for the detection of structural deteriorations of the retino-tectal projection in p50-deficient mice. The MnCl_2 solution was *ivit* injected for transport into the LGN along vital ON fibers, and the signal enhancement was compared between 10-months-old p50 mutant and age-matched WT mice. Analysis of the LGN region revealed that the mean CNR value was significantly reduced by 27% in p50-deficient ($72.6 \pm 6.4\%$; $P<0.01$, $N=8$) compared to WT animals (normalized to $100.0 \pm 4.4\%$, $N=9$) (Fig. 5B). Likewise, the maximum CNR value indicating the peak signal intensity within each LGN was on average 18% reduced in p50-deficient mice. The different signal intensities for anterogradely transported MnCl_2 in the two genotypes is shown as heat map illustrations applied to multi-planar reconstruction images (Fig. 5A). In addition to the reduction of the MEMRI signal, we also observed a significant impairment in visual performance of p50-mutant mice, as demonstrated by visual acuity measurements (WT: 0.376 ± 0.001 , $N=8$; p50 knockout: 0.314 ± 0.003 , $N=6$; $P<0.01$) (Fig. 5C). A detailed characterization of NF- κ B knockout mice

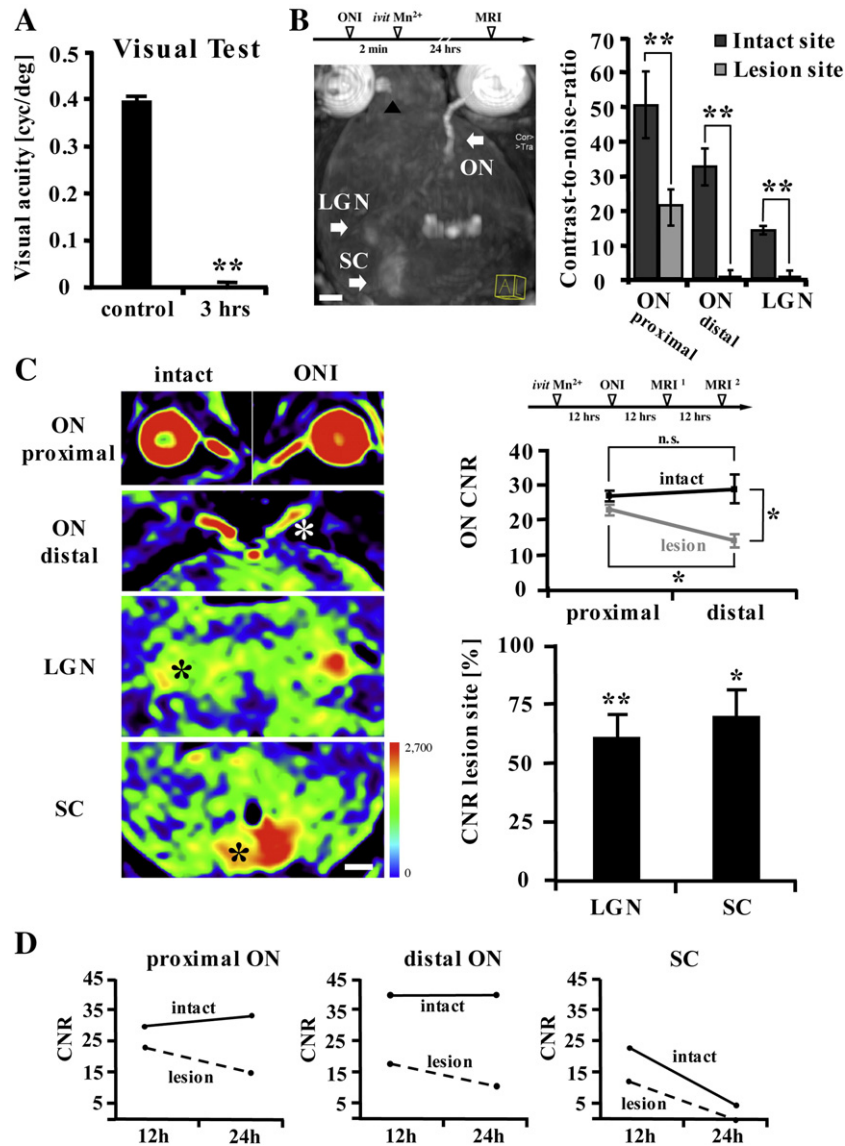


Fig. 3. Temporo-spatial structural and functional degeneration after ONI. (A) Functional test of visual acuity revealed immediate and complete blindness of the animals following acute ONI. Optic nerves (ON) were crushed with a pair of microforceps for 10 s. (B) Left: Multiplanar 3D MIP map of the brain (ventro-lateral view). Complete contrast arrest indicating the injury site 0.8 mm behind the lamina cribrosa (arrow head). In comparison, the retino-tectal projection originating from the left eye remained intact (arrows). Right: CNR calculated from the proximal and distal ON and the LGN of the intact and lesioned projection. (C) Left: Heat map images of the intact and lesioned visual projection 12 h after ONI. Asterisks indicate reduced CNR along the lesioned tract. Right: CNR calculated for the proximal and distal ON, the LGN and SC. Hot colors represent higher MRI signals than cold colors. (D) Kinetic of signal enhancement along the intact and lesioned projection in a representative single animal at 12 and 24 h after ONI. Scale: 1 mm. ***P*<0.01.

by MRI and optometry will be published elsewhere. Thus, MEMRI is also highly sensitive for the detection of even mild, chronic degenerative axonal pathologies and reasonably complements functional tests in mutant mice.

Optometric test

Systemic and cellular toxicity of soluble MnCl₂ administration is well characterized (Moreno et al., 2009; Stanwood et al., 2009). To longitudinally monitor sensory dysfunctions caused by *ivit* application of MnCl₂ we performed visual tests in a virtual-reality optomotor system (Goetze et al., 2010; Prusky et al., 2004), selecting both visual acuity and contrast sensitivity as the most important test parameters. Mice were evaluated 14 days after single, bilateral *ivit* injection of different MnCl₂ dosages thus leaving sufficient time for the development of retinal pathologies. All mice that had obtained a water injection displayed normal visual acuity with a threshold in spatial frequency of

Table 4

CNR data of individually analyzed mouse visual hemiprojections at 12 h and 24 h after uni-lateral crush injury of the Mn²⁺-loaded optic nerves. The reduction of CNR along the ROIs of the injured visual hemiprojection indicates tract degeneration, which was most prominent in distal parts where Wallerian degeneration initiates (also see Fig. 3). N = 4. ROI, region of interest.

Mouse	ROI	Intact		Lesion	
		12 h	24 h	12 h	24 h
1	ON proximal	22.6	30.4	n.d.	12.9
	ON distal	23.9	23.1	19.2	9.9
	SC	12.1	10.1	8.0	6.9
2	ON proximal	26.9	36.4	19.9	19.5
	ON distal	29.4	28.8	10.9	7.1
	SC	19.3	8.3	11.4	3.5
3	ON proximal	27.4	32.4	25.5	18.4
	ON distal	21.1	24.9	13.8	16.0
	SC	7.9	6.2	8.2	4.4
4	ON proximal	29.7	33.1	23.0	14.8
	ON distal	39.6	39.6	17.6	10.4
	SC	22.8	4.4	11.9	-

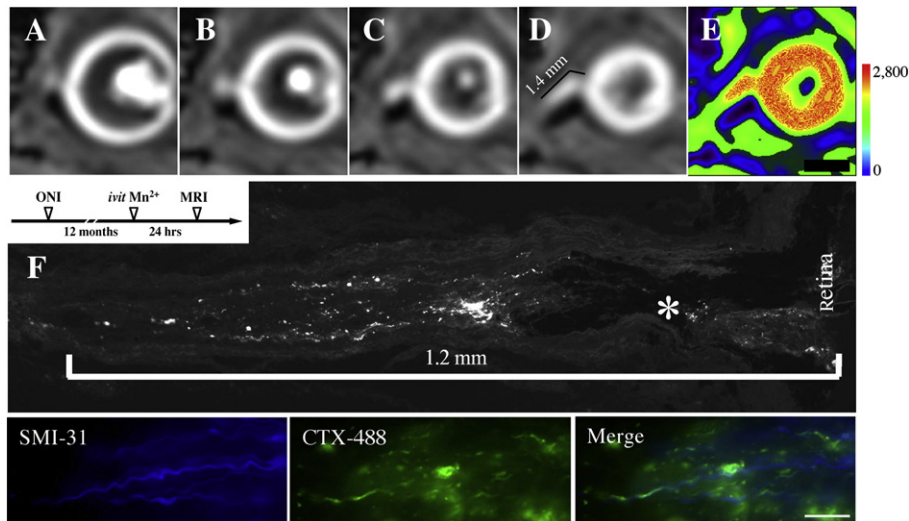


Fig. 4. Detection of axonal regeneration by MEMRI. Regeneration 1 year post-injury in a B6 animal. (A–D) Serial MR images depicting restituted Mn^{2+} transport up to 1.4 mm behind the *lamina cribrosa*. (E) multicolor heat map of (D), where hot colors represent higher MRI signals than cold colors. (F) Longitudinal cryosection through the identical optic nerve 3 days after anterograde labeling. CTX-488 traced newly generated axons up to 1.2 mm behind the disk and co-localized with the phosphorylated neurofilament marker SMI-31. Anterograde CTX-594 applied prior to the injury completely disappeared. Asterisk indicates scar region. Scale: 10 μ m.

0.38 ± 0.001 cyc/deg ($N=12$), similar to values of mice injected with 1.5 or 15 nmol Mn^{2+} (0.38 ± 0.002 cyc/deg, $N=16$) (Fig. 6A). Mean visual acuity was not significantly reduced after application of 50 nmol $MnCl_2$ (0.33 ± 0.04 cyc/deg; $P=0.2$, $N=10$) but dropped drastically and significantly after injecting 100 nmol (0.06 ± 0.06 cyc/deg, $N=6$) or 150 nmol (0.1 ± 0.05 cyc/deg; $P<0.01$, $N=12$). For dosages exceeding 300 nmol $MnCl_2$ ($N=4$) animals did not respond at all to the

presented visual stimuli. Plotting single optometric values for each recorded eye indicated a threshold concentration of 50 nmol beyond which blindness occurred in almost all animals. Thus, unexpectedly, we did not observe a linear dose response curve, but identified a toxic process with a pharmacodynamic “make or break” response beyond the given threshold value (Fig. 6B). Considering severance of macroscopic and histopathologic alterations these effects appeared irreversible.

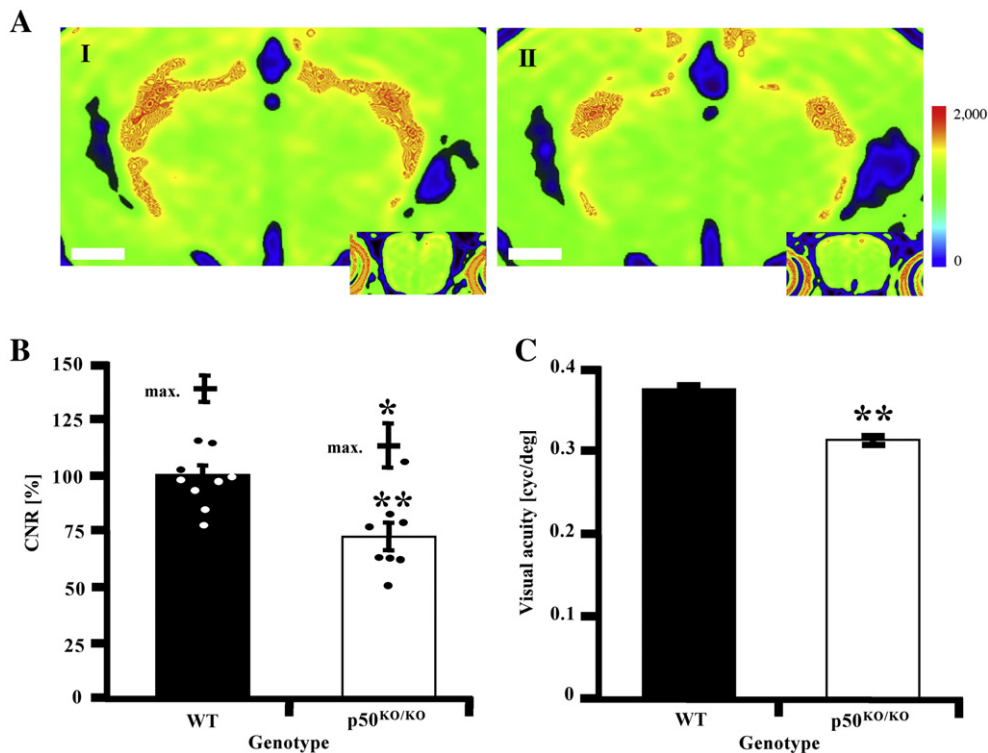


Fig. 5. MEMRI and functional analysis in a model of chronic neurodegeneration. (A) Representative example of a coronal section plane through the LGN in 10-month-old wild-type (WT, I) and NF- κ B p50-deficient ($p50^{KO/KO}$, II) mice. Heat-color images normalized to non-enhanced olfactory bulb area (insert image) show a reduction of the MEMRI signal intensity in p50-deficient mice, which develop chronic ON pathology due to age-dependent RGC death. Hot colors represent higher MRI signals than cold colors. Scale: 1 mm. (B) Quantification of mean and maximum CNR of the LGN in 10-month-old WT and p50-deficient animals. For mean CNR, single data points received from 8 ($p50^{KO/KO}$) and 9 (WT) analyzed visual hemiprojections (circles) and their average values are presented. (C) Visual acuity is significantly reduced in 10-month-old p50-deficient mice compared to age-matched controls. * $P<0.05$; ** $P<0.01$.

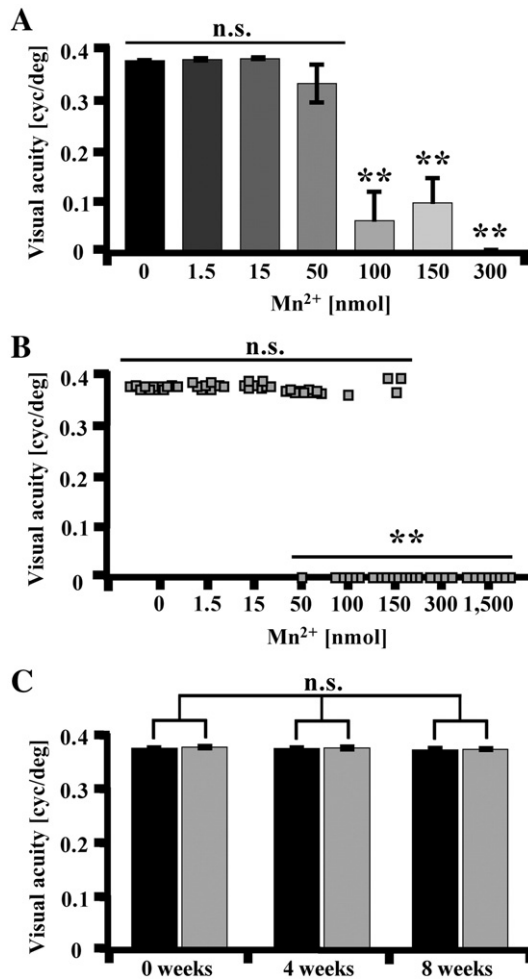


Fig. 6. Optometric assay for MEMRI toxicity in B6 mice. (A) Dosage-dependent decline of visual acuity 14 days after bilateral *ivit* application of Mn²⁺. Dosages up to 15 nmol MnCl₂ did not affect visual function. (B) Plot of single eye visual acuity for the animals shown in (A). All eyes were physiologically intact up to MnCl₂ dosages of 15 nmol, whereas increasing numbers of eyes became blind at higher dosages. (C) Longitudinal study of visual function after *ivit* injection of 15 nmol MnCl₂ (black bars) and water (grey bars), confirming the physiological safety of MEMRI relevant MnCl₂ dosages by a repetitive administration protocol of 6 injections within 8 weeks. **P*<0.05; ***P*<0.01. n.s., not significant.

As a second parameter, contrast sensitivity was monitored for spatial frequencies between 0.031 cyc/deg and 0.272 cyc/deg. All Mn²⁺ injected animals tracked the rotating visual stimuli after dosages of up to 15 nmol, as did water-injected controls (at 0.064 cyc/deg: 15.7 ± 0.4 (0 nmol); 15.6 ± 0.2 (15 nmol); *P* = 0.8). In contrast, at higher dosages, the number of eyes with preserved functionality drastically decreased and more animals completely failed the contrast sensitivity test (not shown).

Since long-term studies require repeated administration of MnCl₂, we validated retinal function after repetitive injections of an MRI contrast-relevant dosage. In total, 6 single injections of 15 nmol MnCl₂ were performed every 2 weeks for 2 months while mouse visual functions were monitored monthly by optometric tests. According to the pharmacokinetic studies referred to above, a time gap of 2 weeks was sufficient to completely clear MnCl₂ from the visual projection. As shown in Fig. 6C, visual acuity (0.380 ± 0.002) remained unimpaired after repetitive MnCl₂ injections for 4 (0.379 ± 0.002; *P* = 0.7, *N* = 8) and 8 weeks (0.376 ± 0.001; *P* = 0.1, *N* = 8) thereafter. Correspondingly, contrast sensitivity was completely unaffected after repetitive injections of 15 nmol Mn²⁺ in each tested animal (4 weeks: *P* = 1.0; 8 weeks: *P* = 0.9). Thus, *ivit* applications of Mn²⁺ at MRI contrast-

relevant dosages proved physiologically safe and were free of obvious cumulative toxic effects when administered in intervals of 2 weeks.

Histopathology

After *ivit* MnCl₂ injections, MEMRI analysis and functional optomotor tests, retinae were analyzed for RGC toxicity by beta-III tubulin (TUJ-1) immunostaining on flat mounted specimens (Fig. 7B, circles). As expected, RGC density averaged at 3600 ± 172/mm² (*N* = 6) for water-injected control eyes. Application of 15 nmol Mn²⁺ did not affect RGC density (3598 ± 201/mm²; *P* = 0.99, *N* = 4). At 50 nmol (2828 ± 231/mm², *N* = 4) and 100 nmol (2854 ± 269/mm², *N* = 4) RGC density was slightly, but significantly reduced by 21.5% and 20.7%, respectively (*P* < 0.05). We observed a further reduction in RGC survival by 31.0% after exposure to 150 nmol. However, almost 70% (2483 ± 470/mm²; *P* < 0.05, *N* = 5) of the basal RGC density remained present and morphology of the RGC layer appeared normal. Obviously, MnCl₂-induced decline in RGC numbers was not sufficient to explain the rigorous loss of visual functionality observed in the optometric assay. Since we found progressive atrophy of the retinal diameter with increasing MnCl₂ dosages retinal morphology was analyzed in detail (Fig. 7A, left row). After *ivit* injections of 15 nmol Mn²⁺, the characteristic cell layers appeared well organized and of proper thickness as in water-injected control eyes. In contrast, after *ivit* injections of 50 nmol MnCl₂, the outer nuclear layer (ONL) was barely detectable and completely disappeared in 100 nmol samples, resulting in a significant reduction of the overall retinal thickness (Fig. 7A). To confirm a MnCl₂-induced specific degeneration of the ONL, which mainly consists of photoreceptors (PR), we prepared immunofluorescence stainings of recoverin-expressing PR (McGinnis et al., 1999) and measured the composite thickness of the inner and outer segments. Both the cell nucleus comprising inner segment as well as the disks of rods and membraneous foldings of cones bearing outer segments were selectively labeled in retinal sections after 0 nmol and 15 nmol Mn²⁺ spanning 127.0 ± 3.8 μm and 126.0 ± 9.3 μm (*P* = 0.9), respectively (Fig. 7A, third row). In 50 nmol *ivit* MnCl₂ retinae, the recoverin-positive layers of the inner and outer PR segments were shrunk to 55.0 ± 9.4 μm (*P* < 0.01) and after 100 nmol *ivit* MnCl₂ only scattered cell bodies without disk areas were detectable (7.9 ± 0.6 μm; *P* < 0.01) (Fig. 7B, bars). Furthermore, immunohistochemical examination of glial cell populations identified enhanced immunoreactivity for the astrogliosis marker glial fibrillary acidic protein (GFAP) in astrocytes of the GCL (not shown) along with a notable loss of cellular retinaldehyde-binding protein (CRALBP) expression in Muller glia end feet (Suppl. Fig. 2) at 50 nmol and, particularly, at 100 nmol MnCl₂.

Discussion

There is increasing demand for high resolution *in vivo* imaging of neuronal circuits and reasonable visualization of fiber projections within the intact and pathologic brain. This need is reflected by recent technical innovations, such as ultramicroscopy developed by Dodt et al. (2007), which enables experimental illustration of complete neuronal networks inside the mouse brain. The advantage of this method is the superb quality in cellular resolution. However, since it requires tissue fixation it cannot be applied on living animals (Dodt et al., 2007). A non-invasive methodology for repetitive *in vivo* picturing in rodents and humans represents voxel-based, DWI-deduced DTI (diffusion tensor imaging), which assesses the amplitude and directionality of water molecules diffusing along white matter tracts. DTI deduced, highly developed DTT (diffusion tensor tractography) protocols reconstruct trajectories by tracking the direction of fastest water diffusion and their correspondence to the longitudinal axis of the tract. Apart from this, high resolution MRI of small animals is more and more becoming a method of choice for neuro-scientific studies to detect and monitor structural peculiarities of the injured, aging and

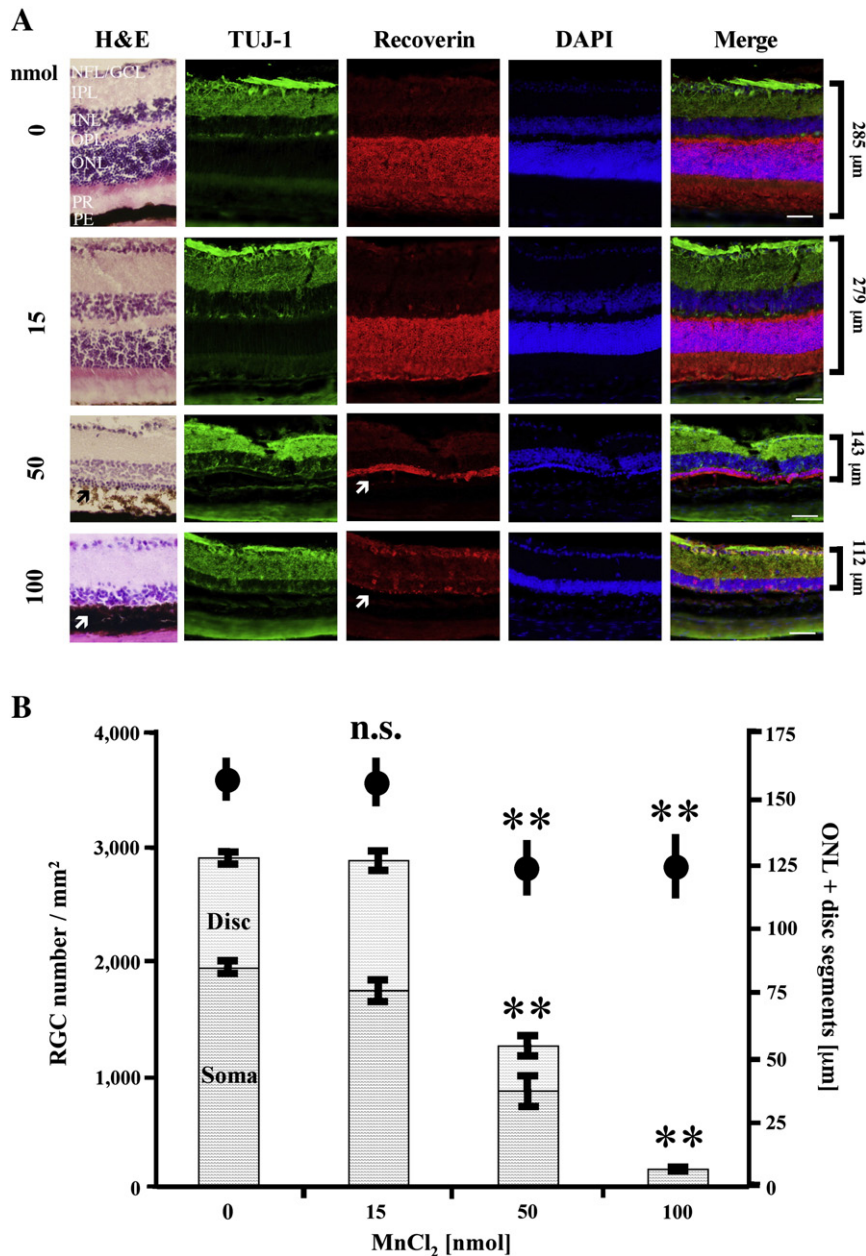


Fig. 7. Cellular toxicity of *ivit* applied MnCl₂ in mouse retina. (A) Histological sections show normal cell layer morphology (H&E, left). Immunohistochemical stainings of photoreceptors (PR) of the outer nuclear layer (ONL) with recoverin, and of the ganglion cell layer (GCL) and the optic nerve fiber layer (NFL) with TUJ-1 showed a physiologic pattern in control and 15 nmol MnCl₂ treated retinæ. At 100 nmol MnCl₂, the diameter of the ONL was drastically reduced (arrow). The GCL and NFL showed no gross morphologic alteration. For layer orientation, slices were counterstained with the nuclear marker DAPI. (B) Measurement of RGC numbers (circles) and thickness of the inner and outer segment of the ONL (bars). Mn²⁺-induced toxicity above dosages of 15 nmol preferentially affected PR survival and less RGC survival. Scale: 50 μm; ***P*<0.01.

pathologic brain. Advances in conventional MRI techniques implement the use of Mn²⁺ as a contrast-enhancing compound (MEMRI). In contrast to standard Gd-DTPA that necessitates its intravenous administration it can be applied loco-regionally into the tissue in order to investigate CNS activity, demyelination, or inflammatory states (Boretius et al., 2008; Yu et al., 2005). Whereas MnCl₂ shortens T1 relaxation time in any actively transporting axons, Gd-DTPA penetrates into the tissue and reduces T1 only at the site of the collapsed BBB. In contrast to histological studies, it allows serial investigations on living individual animals and the acquisition time is much lower than e.g. by DTI techniques. To facilitate MEMRI imaging in animals, ultra-high field animal scanners with an extraordinarily high spatial resolution of up to 30 μm or even higher and excellent tissue contrast have been used. In many laboratories, however, clinical whole-body scanners are the only accessible, and well-established

scan protocols are hardly transferrable to dedicated animal scanners. Further, conventional low field scanners much better preserve the contrasting effects of many T1-shortening agents such as Gd-DTPA and Mn²⁺ as their relaxation (R1) is field dependent and typically reduced at very high field strength (Morgan and Nolle, 1959). More essentially, the SNR loss by approximately a factor of 3 in low as compared to high field scanners impairs image quality. However, this can be compensated by repetitive, time consuming averaging. With all the ameliorations commonly practicable such as the use of optimal sequences, sequence parameters and adequate coils, the clinical 3 T scanner achieves a resolution of isotropic (0.2 mm)³ at an acceptable SNR.

Here, we used MnCl₂ as a T1 shortening agent to realize contrast enhanced high-resolution multiplanar imaging of the visual projection in a clinical 3 T scanner. MIPs, which are commonly used in MR time-of-

flight (TOF) angiography protocols allowed a precise 3D reconstruction of the entire retino-tectal projection. As for hardware conditions, a small loop coil with a linearly polarized Litz volume resonator that provides a homogeneous FoV of 33 mm in axial direction (Doty et al., 2007) allowed for additional gain on SNR and CNR (own unpublished observations). Employing a 3D FLASH gradient echo sequence at TE/TR 6.51/16 ms and a Flip angle of 22° with 2 averages and 3 repetitions we could realize a total acquisition time of 30–35 min, which is much shorter than standard DTI scan time (several hours). With this acquisition time, fast axonal dynamics are indeed not resolvable. However, the typical time scales found for Mn^{2+} transport in our paradigm were in the range of hours. Accounting for optimum contrast in target tissues, Mn^{2+} application parameters were adjusted to the special mouse situation by precedent pharmacokinetic studies (Figs. 1B and C) and showed clear differences as compared to rats (Thuen et al., 2005). At present, only limited information is available for dosage and sensitivity of MEMRI in mice (Bearer et al., 2007; Lindsey et al., 2007). The narrow time and dose responses for mice found in our detailed, large-scale studies (N=58) were translated into applicable, reproducible protocols for longitudinal studies of axonal degeneration and regeneration in the mouse visual system.

Using this protocol, key structures of the retino-tectal projection were clearly discernable from background tissue with high reproducibility and resolution. Distinct Mn^{2+} accumulation occurred exclusively in parts of the visual projection, i.e. the ipsilateral retina and ON, the optic chiasm as decussation point of ~95% of RGC axons in pigmented mice, as well as the contralateral presynaptic thalamic LGN and midbrain SC. Similar to the conditions in rats (Thuen et al., 2005), the intracerebral small fraction of uncrossed fibers (less than 5% ipsilateral in non-albinos) could not be resolved using the 3 T scanner. Moreover, we did not see evidence for additional trans-synaptic Mn^{2+} propagation into visual cortical areas even under particular focus of tracer enrichment in V1 and V2 projection areas and the V4 relay area of the occipital visual cortex under augmented Mn^{2+} dosage. The minimal increase in signal enhancement beyond two synaptic junctions referred by Lindsey et al. (2007) might reach detection threshold only in a 7 Tesla field. Bearer and colleagues found reduced Mn^{2+} -enhancement in the LGN and SC of blind animals, suggesting that trans-synaptic transport depends on electrical activity. However, enrichment in areas posterior to the LGN, i.e. along geniculostriate projections remained out of focus of investigation (Bearer et al., 2007). Biologically, activity dependent trans-synaptic propagation requires Mn^{2+} release into the synaptic cleft, its uptake via calcium channels at the post-synaptic membrane concomitant with nerve cell depolarization and further axonal transport. The well-confirmed appearance of trans-synaptic Mn^{2+} transmission in rats (Thuen et al., 2005; Watanabe et al., 2001) might thus be due to species dependent differences in ion uptake, transport and release. Indeed, even other groups critically discuss the occurrence of trans-synaptic transport in mice (Pautler, 2004; Takeda et al., 1998).

The toxicity of $MnCl_2$ is well documented and associated with clinical symptoms of Parkinson disease and neuropsychiatric and cognitive alterations. Therefore, the aim of broad and *in vivo* administration of MEMRI undoubtedly necessitates detailed expertise on tracer dosages, substrate pharmacokinetics, and cell specific toxicity. As described for rats, directly exposed RGC died at doses beyond 300 nmol of *ivit* injected Mn^{2+} (Thuen et al., 2008). In mice, Mn^{2+} toxicity on RGC was examined by VEP recordings after *ivit* injection of various volumes and dosages (Bearer et al., 2007). Whereas visually evoked potentials completely recovered from transient depression after exposure to low volumes of about 7 nmol, amplitudes remained diminished after application of higher dosages (100 nmol) 24 h thereafter (Bearer et al., 2007). Here, we show that dosages in the low nmol range (15–50 nmol) are physiologically and ultrastructurally safe as demonstrated by functional tasks and histologic parameters. However, dosages above 50 nmol caused significant pathology of the eye and retina such as ocular phthisis,

intraretinal bleeding and lens opaqueness, reflecting the narrow physiological scope of Mn^{2+} . Such a concentration-dependent non-linear pharmacodynamic with a “make or brake” threshold is typical for toxic compounds and clinically relevant when a therapeutic range is searched and undesirable side effects have to be prevented. Notably, cumulative toxicity was avoided by appropriate injection intervals that allowed entire washout of the tracer. Likewise, preceding kinetic studies had depicted almost complete clearance of Mn^{2+} from the retina 5 days after tissue inoculation. Apart from RGC apoptosis and electrophysiological VEP recordings, our histopathological studies evaluated the impact of Mn^{2+} on individual retinal cell populations, i.e. RGCs, photoreceptors (PR) and Muller glia and the overall retinal architecture. Cell-type specific pathology was then correlated to functional tasks on visual acuity and contrast sensitivity. Therewith, performance on visual acuity may subtly reflect RGC activity, and contrast discrimination is thought to be a function of RGC and PR, suggesting these methods to be sensitive enough to rule out even mild noxious effects. This seems important as the broad and refined application of Mn^{2+} on sensory projections, on forebrain areas and basal nuclei warrants detailed knowledge on cell type-specific susceptibility. Our histopathological studies revealed that beyond the threshold concentration of 50 nmol PR are most sensitive to Mn^{2+} toxicity followed by Muller glia, whereas RGC and interneurons appeared more resistant against Mn^{2+} -induced cell pathology and death. This may be due to the high energy need and metabolic turnover in PR. Physiologically, calcium homeostasis of PR is primarily regulated by their outer segments affording hyperpolarization of the cell membrane, and calcium influx at the synapse by voltage-gated calcium channels regulates glutamate release and trans-synaptic stimulation of connected neurons. Histopathologically, particularly the disk areas of the outer segments showed progressive destruction suggesting that severely impaired phototransduction caused the fatal functional phenotype. Pathophysiologically, as a calcium analog, excess concentrations of Mn^{2+} may liberate excitotoxic cascades by uncontrolled vesicular transport and surplus release of glutamate at the highly active ribbon synapses. Strong intraretinal MEMRI signals indeed suggested accumulation of Mn^{2+} within the affected cell groups. Beside considerations of metabolic turnover, RGC may express subsets of calcium channels, which do not allow for Mn^{2+} transport. Further, in Muller glia we observed a reactive loss of the substrate-routing protein cellular retinaldehyde-binding protein (CRALBP), which influences the enzymatic partitioning of 11-cis-retinol at a key branch point in the visual cycle. Muller glia may respond equally susceptible to Mn^{2+} due to their high metabolic activity as well as the calcium dependence of their nutritive and homeostatic activity. Drastic deteriorations in visual capacity observed after exposure to toxic Mn^{2+} doses are thus most likely due to PR dysfunction and loss rather than a pathology of quite inactive RGC whose numbers were only moderately impaired. Notably, even a protective effect on injured RGC by non-toxic Mn^{2+} dosages have been described in rats, possibly mediated by scavenge of free radicals (Thuen et al., 2009). Further electrophysiological studies may help to elucidate $MnCl_2$ -related damage to specific cell populations within the retina and brain.

In an acute crush model of the ON, we investigated the capability of Mn^{2+} to detect axonal damage. To minimize lesion-mediated artifacts by inflammation, closed crush injury was preferred over surgical exposition and open crush performance. In this paradigm, complete arrest of Mn^{2+} transport due to mechanical breakage of axonal microtubules without damage to the myelin sheaths emphasized the selectiveness of the assumed axonal propagation mechanism. In contrast to the signal increment in the proximal nerve stump described within the earliest 24 h after crush injury in rats, which was interpreted as tracer accumulation at the very end of the interrupted axons (Thuen et al., 2005), we observed a CNR decrease by approximately 60%. This may possibly point to different calcium transporter densities between these two species or be related to the

discrepant crush models applied. Further, solely after axotomy, but not crush injury, calcium influx through the lesion site may contribute to increased tracer enrichment. Commonly, axonal degeneration is supposed to be accompanied by an increase of intra-axonal calcium (Mata et al., 1986) contributed by its delimitation from intra-axonal stores, its redistribution along Schmidt–Lanterman incisures, or by influx via voltage-dependent calcium channels. In inflamed ON of an EAE model, increase of signal intensity of ON axons 24 h after systemic Mn^{2+} application correlated with the loss of axons (Boretius et al., 2008). Moreover and contradictory to the suggested signal increment, we detected rapid tracer fading all along the visual projection after acute crush injury of the ON. CNR values pointed to an onset of tracer loss in very distal subcortical projection areas (SC) where Wallerian degeneration is estimated to originate (Coleman, 2005). The rapid kinetic of tracer loss exceeded the physiological clearance velocity of $MnCl_2$ calculated in our preceding kinetic studies. At present, we do not know whether this is due to an early dysfunction of ion exchangers along the axolemma or increased Mn^{2+} clearance by capillary leakage. More likely, early Wallerian degeneration in absence of an inflammatory or excitatory stimulus may contribute to this fading phenomenon. In presence of an intact BBB that sufficiently impedes ion diffusion, signal attenuation by a loss of axonal density or activity might dominate over increases in intracellular calcium shifts. MEMRI signal attenuation under non-inflammatory acute axonal degeneration thus shows analogy to T1 reduction after myelin and axon loss, commonly described as “dark holes” in MRI.

In 10-months-old NF- κ B p50-deficient mice, which served as model for chronic retino-fugal degeneration, we found a significant reduction of mean and maximum CNR in the LGN compared to age-matched wild-type animals. Recently, it has been shown that such mice with homozygous deletion of the NF- κ B p50 subunit develop spontaneous optic neuropathy and an age-dependent loss of RGC (Takahashi et al., 2007). In this mutant, RGC densities are still normal in 3 weeks and 2 months young mice, but their numbers decrease by about 20% in 5-months-old animals. Coincident with the degeneration of RGCs, the number of RGC axons in the ON homogeneously declines. Therefore, we suggest that the decrease in ON axons as origin of the retino-recipient projection results in an overall reduced axonal Mn^{2+} transport along the presynaptic part of the visual projection and in reduced Mn^{2+} accumulation in the LGN. The sensitivity of the MEMRI method seems sufficient to detect this subtle atrophic process of an isolated CNS projection. Considering the unresolvable 4% of RGC axons of the healthy ipsilateral projection and assuming an RGC axon loss of about 20% in the $p50^{KO/KO}$, the threshold of resolution with a 3 T scanner at a RGC density of 70,000 makes between 3000 and 14,000 myelinated axons. Although we cannot completely exclude a pan-neuronal dysfunction, the reduced MEMRI signal intensity is most likely due to the histopathological phenotype reported for this mouse line. Ongoing experiments on detailed structural, functional and histological characterizations of subunit-specific NF- κ B knockouts will elucidate this topic in the future. The severe reduction of visual functions as assessed by visual tasks in our p50-deficient mice at an

assumed moderate loss of less than 50% of RGC suggests impairment in both, axonal number and function to contribute to MEMRI signal attenuation. That MEMRI also reflects fMRI-like functions of spatial and temporal activity and plasticity has nicely been demonstrated for tonotopic auditory brain mapping (Yu et al., 2005).

For regeneration studies, MEMRI was performed 12 months after crush injury and anterograde tracer preparation. We detected limited spontaneous regeneration of few axons extending from the optic disk up to 1.4 mm within the preserved nerve sheath. MEMRI was capable to detect such limited regeneration as indicated by the reconstituted signal reinforcement in the proximal ON stump. We found a high correlation between the absolute spatial extent of MEMRI signal restitution and growth distance measured on identical serial longitudinal cryosections (1.2 versus 1.4 mm). The limited growth dimensions are in accordance with the lack of abundant or long-distance regeneration under naïve conditions in the CNS of adult mammals, suggesting that myelin-derived growth inhibitors such as Nogo, OMgp and MAG and glial scar constituents impede effective regeneration. Under stimulated conditions, e.g. after peripheral nerve grafting, trans-lesional regeneration up to 3 mm was detected in rats by the use of a 7 Tesla scanner (Thuen et al., 2009). At present, we are confirming our growth results in mice with genetically stimulated regeneration. With immediate effect, the protocol established seems sensitive enough to detect low-level regeneration in mice and to visualize rewiring processes after CNS injury as recently pioneered by Ghosh et al. (2010).

In summary, this technique may prove highly useful to locate developmental and disease-derived pathological alterations of tract fiber proportions and fiber integrity, e.g. between pigmented and albino rodents and in mutated animals mimicking hereditary or sporadic neurodegenerative diseases. Moreover, this study aimed to support access to a plethora of transgenic and pharmaceutically treated mice in order to allow longitudinal screenings of their structural phenotypes. Prospectively, the technique might prove advantageous in a range of other experimental models such as spinal cord injury (Simonen et al., 2003) or facial nerve transection (Guntinas-Lichius et al., 2007). In particular, the use of chelated, clinically already approved Mn^{2+} derivatives in the brain would be a breakthrough as means for diagnostic and therapeutic control. Further studies will reveal whether MEMRI can account for critical links between conventional neurobiological techniques and functional characterization of neuronal circuits, e.g. by behavioral tests or electrophysiological measurements (Fig. 8) and thus strengthen our comprehension for structural and functional interplay.

Abbreviations

ON	optic nerve
ONI	optic nerve injury
CNR	contrast-to-noise ratio
CNS	central nervous system
CRALBP	cellular retinaldehyde-binding protein

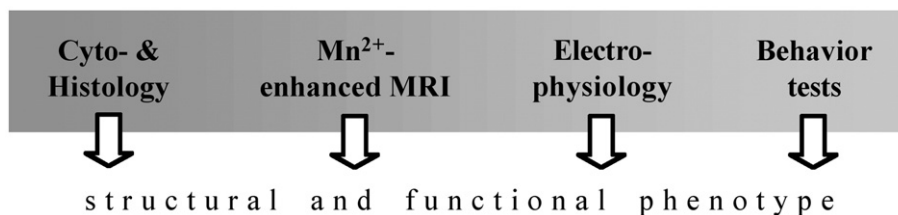


Fig. 8. Integration of MEMRI into classic neurobiological methodology. Mn^{2+} -induced signal enhancement allows for qualitative and quantitative evaluation of CNS projections. Supplementary to histological sections, the topography of specific fiber tracts can be visualized by Mn^{2+} -enhancement *in vivo*. When assigned as Ca^{2+} analog, Mn^{2+} -induced signal enhancement in axonal targets may serve as indicator of vitality and electric activity.

CTX	cholera toxin
Cyc/deg	cycle per degree
3D	three-dimensional
DTI	diffusion tensor imaging
DTT	diffusion tensor tractography
DWI	diffusion weighted imaging
fMRI	functional MRI
GCL	ganglion cell layer
GFAP	glial fibrillary acidic protein
Ivit	intravitreal injection
LGN	lateral geniculate nucleus
MEMRI	manganese enhanced MRI
MIP	maximum intensity projection
MRI	magnetic resonance imaging
NF- κ B	nuclear factor kappa B
ON	optic nerve
ONL	outer nuclear layer
PR	photo receptor
RGC	retinal ganglion cell
ROI	region of interest
SC	superior colliculus
SNR	signal-to-noise ratio
TOF	time of flight

Supplementary data associated with this article can be found, in the online version, at doi:10.1016/j.neuroimage.2011.07.069.

Acknowledgments

We thank I. Krumbein and S. Tausch for technical support.

References

- Bearer, E.L., Falzone, T.L., Zhang, X., Biris, O., Rasin, A., Jacobs, R.E., 2007. Role of neuronal activity and kinesin on tract tracing by manganese-enhanced MRI (MEMRI). *Neuroimage* 37, 37–46.
- Benowitz, L., Yin, Y., 2008. Rewiring the injured CNS: lessons from the optic nerve. *Exp. Neurol.* 209, 389–398.
- Berry, M., Carille, J., Hunter, A., Tsang, W., Rosenstiel, P., Sievers, J., 1999. Optic nerve regeneration after intravitreal peripheral nerve implants: trajectories of axons regrowing through the optic chiasm into the optic tracts. *J. Neurocytol.* 28, 721–741.
- Boretius, S., Gadajski, I., Demmer, I., Bähr, M., Diem, R., Michaelis, T., Frahm, J., 2008. MRI of optic neuritis in a rat model. *Neuroimage* 41, 323–334.
- Chan, K.C., Li, J., Kau, P., Zhou, I.Y., Cheung, M.M., Lau, C., Yang, J., So, K., Wu, E.X., 2011. *In vivo* retinotopic mapping of superior colliculus using manganese-enhanced magnetic resonance imaging. *Neuroimage* 54, 389–395.
- Coleman, M., 2005. Axon degeneration mechanisms: commonality amid diversity. *Nat. Rev. Neurosci.* 6, 889–898.
- Doty, H.U., Leischner, U., Schierloh, A., Jähring, N., Mauch, C.P., Deininger, K., Deussing, J.M., Eder, M., Zieglgänsberger, W., Becker, K., 2007. Ultramicroscopy: three-dimensional visualization of neuronal networks in the whole mouse brain. *Nat. Methods* 4, 331–336.
- Doty, F.D., Entzminger, G., Kulkarni, J., Pamarthy, K., Staab, J.P., 2007. Radio frequency coil technology for small-animal MRI. *NMR Biomed.* 20, 304–325.
- Dräger, U.C., Olsen, J.F., 1980. Origins of crossed and uncrossed retinal projections in pigmented and albino mice. *J. Comp. Neurol.* 191, 383–412.
- Ferri, A., Sanes, J.R., Coleman, M.P., Cunningham, J.M., Kato, A.C., 2003. Inhibiting axon degeneration and synapse loss attenuates apoptosis and disease progression in a mouse model of motoneuron disease. *Curr. Biol.* 13, 669–673.
- Franklin, K.B.J., Paxinos, G., 1997. *The Mouse Brain in Stereotaxic Coordinates*. Academic Press.
- Ghosh, A., Haiss, F., Sydecum, E., Schneider, R., Gullo, M., Wyss, M.T., Mueggler, T., Baltes, C., Weber, B., Schwab, M.E., 2010. Rewiring of hindlimb corticospinal neurons after spinal cord injury. *Nat. Neurosci.* 13, 97–104.
- Goetze, B., Schmidt, K.F., Lehmann, K., Altrock, W.D., Gundelfinger, E.D., Löwel, S., 2010. Vision and visual cortical maps in mice with a photoreceptor synaptopathy: reduced but robust visual capabilities in the absence of synaptic ribbons. *Neuroimage* 49, 1622–1631.
- Guntinas-Lichius, O., Hundeshagen, G., Paling, T., Streppel, M., Grosheva, M., Irintchev, A., Skouras, E., Alvanou, A., Angelova, S.K., Kuerten, S., Sinis, N., Dunlop, S.A., Angelov, D.N., 2007. Manual stimulation of facial muscles improves functional recovery after hypoglossus-facial anastomosis and interpositional nerve grafting of the facial nerve in adult rats. *Neurobiol. Dis.* 28, 101–112.
- Hayhow, W.R., Sefton, A., Webb, C., 1962. Primary optic centers of the rat in relation to the terminal distribution of the crossed and uncrossed optic nerve fibers. *J. Comp. Neurol.* 118, 295–321.
- Howles, G.P., Bing, K.F., Qi, Y., Rosenzweig, S.J., Nightingale, K.R., Johnson, G.A., 2010. Contrast-enhanced *in vivo* magnetic resonance microscopy of the mouse brain enabled by noninvasive opening of the blood–brain barrier with ultrasound. *Magn. Reson. Med.* 64, 995–1004.
- Isemann, S., Schmeer, C., Kretz, A., 2004. How to keep injured CNS neurons viable—strategies for neuroprotection and gene transfer to retinal ganglion cells. *Mol. Cell. Neurosci.* 26, 1–16.
- Kim, J., Choi, I.-Y., Michaelis, M.L., Lee, P., 2011. Quantitative *in vivo* measurement of early axonal transport deficits in a triple transgenic mouse model of Alzheimer's disease using manganese-enhanced MRI. *Neuroimage* 56, 1286–1292.
- Kretz, A., Happold, C.J., Marticke, J.K., Isemann, S., 2005. Erythropoietin promotes regeneration of adult CNS neurons via Jak2/Stat3 and PI3K/AKT pathway activation. *Mol. Cell. Neurosci.* 29, 569–579.
- Lehmann, K., Löwel, S., 2008. Age-dependent ocular dominance plasticity in adult mice. *PLoS One* 3, e3120.
- Libby, R.T., Li, Y., Savinova, O.V., Barter, J., Smith, R.S., Nickells, R.W., John, S.W., 2005. Susceptibility to neurodegeneration in glaucoma is modified by Bax gene dosage. *PLoS Genet.* 1, 17–26.
- Lindsey, J.D., Scadeng, M., Dubowitz, D.J., Crowston, J.G., Weinreb, R.N., 2007. Magnetic resonance imaging of the visual system *in vivo*: transsynaptic illumination of V1 and V2 visual cortex. *Neuroimage* 34, 1619–1626.
- Mata, M., Staple, J., Fink, D.J., 1986. Changes in intra-axonal calcium distribution following nerve crush. *J. Neurobiol.* 17, 449–467.
- McGinnis, J.F., Stepanik, P.L., Chen, W., Elias, R., Cao, W., Lerioux, V., 1999. Unique retina cell phenotypes revealed by immunological analysis of recoverin expression in rat retinal cells. *J. Neurosci. Res.* 55, 252–260.
- Mendonca-Dias, M.H., Gaggelli, E., Lauterbur, P.C., 1983. Paramagnetic contrast agents in nuclear magnetic resonance medical imaging. *Semin. Nucl. Med.* 13, 264–376.
- Moreno, J.A., Yeomans, E.C., Streifel, K.M., Brattin, B.L., Taylor, R.J., Tjalkens, R.B., 2009. Age-dependent susceptibility to manganese-induced neurological dysfunction. *Toxicol. Sci.* 112, 394–404.
- Morgan, L.O., Nolle, A.W., 1959. Proton spin relaxation in aqueous solutions of paramagnetic ions. II. Cr, Mn, Ni, Cu, and Gd. *J. Chem. Phys.* 31, 356–368.
- Olsen, Ø., Thuen, M., Berry, M., Kovalev, V., Petrou, M., Goa, P.E., Sandvig, A., Haraldseth, O., Brekken, C., 2008. Axon tracing in the adult rat optic nerve and tract after intravitreal injection of MnDPDP using a semiautomatic segmentation technique. *J. Magn. Reson. Imaging* 27, 34–42.
- Pautler, R.G., 2004. *In vivo*, trans-synaptic tract-tracing utilizing manganese-enhanced magnetic resonance imaging (MEMRI). *NMR Biomed.* 17, 595–601.
- Pautler, R.G., Koretsky, A.P., 2002. Tracing odor-induced activation in the olfactory bulbs of mice using manganese-enhanced magnetic resonance imaging. *Neuroimage* 16, 441–448.
- Pautler, R.G., Silva, A.C., Koretsky, A.P., 1998. *In vivo* neuronal tract tracing using manganese-enhanced magnetic resonance imaging. *Magn. Reson. Med.* 40, 740–748.
- Pautler, R.G., Mongeau, R., Jacobs, R.E., 2003. *In vivo* trans-synaptic tract-tracing from the murine striatum and amygdala utilizing manganese-enhanced MRI (MEMRI). *Magn. Reson. Med.* 50, 33–39.
- Prusky, G.T., Alam, N.M., Beekman, S., Douglas, R.M., 2004. Rapid quantification of adult and developing mouse spatial vision using a virtual optomotor system. *Invest. Ophthalmol. Vis. Sci.* 45, 4611–4616.
- Sha, W.C., Liou, H.C., Tuomanen, E.I., Baltimore, D., 1995. Targeted disruption of the p50 subunit of NF- κ B leads to multifocal defects in immune responses. *Cell* 80, 321–330.
- Simonen, M., Pedersen, V., Weinmann, O., Schnell, L., Buss, A., Ledermann, B., Christ, F., Sansig, G., van der Putten, H., Schwab, M.E., 2003. Systemic deletion of the myelin-associated outgrowth inhibitor Nogo-A improves regeneration and plastic responses after spinal cord injury. *Neuron* 38, 201–211.
- Stanwood, G.D., Leitch, D.B., Savchenko, V., Wu, J., Fitsanakis, V.A., Anderson, D.J., Stankowski, J.N., Aschner, M., McLaughlin, B.A., 2009. Manganese exposure is cytotoxic and alters dopaminergic and GABAergic neurons within the basal ganglia. *J. Neurochem.* 110, 378–389.
- Stokin, G.B., Lillo, C., Falzone, T.L., Brusch, R.G., Rockenstein, E., Mount, S.L., Raman, R., Davies, P., Masliah, E., Williams, D.S., Goldstein, L.S., 2005. Axonopathy and transport deficits early in the pathogenesis of Alzheimer's disease. *Science* 307, 1282–1288.
- Takahashi, Y., Katai, N., Murata, T., Taniguchi, S.I., Hayashi, T., 2007. Development of spontaneous optic neuropathy in NF- κ Bp50-deficient mice: requirement for NF- κ Bp50 in ganglion cell survival. *Neuropathol. Appl. Neurobiol.* 33, 692–705.
- Takeda, A., Kodama, Y., Ishiwatari, S., Okada, S., 1998. Manganese transport in the neural circuit of rat CNS. *Brain Res. Bull.* 45, 149–152.
- Thuen, M., Singstad, T.E., Pedersen, T.B., Haraldseth, O., Berry, M., Sandvig, A., Brekken, C., 2005. Manganese-enhanced MRI of the optic visual pathway and optic nerve injury in adult rats. *J. Magn. Reson. Imaging* 22, 492–500.
- Thuen, M., Berry, M., Pedersen, T.B., Goa, P.E., Summerfield, M., Haraldseth, O., Sandvig, A., Brekken, C., 2008. Manganese-enhanced MRI of the rat visual pathway: acute neural toxicity, contrast enhancement, axon resolution, axonal transport, and clearance of Mn(2+). *J. Magn. Reson. Imaging* 28, 855–865.
- Thuen, M., Olsen, O., Berry, M., Pedersen, T.B., Kristoffersen, A., Haraldseth, O., Sandvig, A., Brekken, C., 2009. Combination of Mn²⁺-enhanced and diffusion tensor MR imaging gives complementary information about injury and regeneration in the adult rat optic nerve. *J. Magn. Reson. Imaging* 29, 39–51.

- Tillet, Y., Batailler, M., Thibault, J., 1993. Neuronal projections to the medial preoptic area of the sheep, with special reference to monoaminergic afferents: immunohistochemical and retrograde tract-tracing studies. *J. Comp. Neurol.* 330, 195–220.
- Tofts, P.S., Porchia, A., Jin, Y., Roberts, R., Berkowitz, B.A., 2010. Toward clinical application of manganese-enhanced MRI of retinal function. *Brain Res. Bull.* 81, 333–338.
- Watanabe, T., Michaelis, T., Frahm, J., 2001. Mapping of retinal projections in the living rat using high-resolution 3D gradient-echo MRI with Mn^{2+} -induced contrast. *Magn. Reson. Med.* 46, 424–429.
- Watanabe, T., Natt, O., Boretius, S., Frahm, J., Michaelis, T., 2002. In vivo 3D MRI staining of mouse brain after subcutaneous application of $MnCl_2$. *Magn. Reson. Med.* 48, 852–859.
- Watanabe, T., Frahm, J., Michaelis, T., 2004a. Functional mapping of neural pathways in rodent brain in vivo using manganese-enhanced three-dimensional magnetic resonance imaging. *NMR Biomed.* 17, 554–568.
- Watanabe, T., Radulovic, J., Spiess, J., Natt, O., Boretius, S., Frahm, J., Michaelis, T., 2004b. In vivo 3D MRI staining of the mouse hippocampal system using intracerebral injection of $MnCl_2$. *Neuroimage* 22, 860–867.
- Watanabe, T., Frahm, J., Michaelis, T., 2008. Manganese-enhanced MRI of the mouse auditory pathway. *Magn. Reson. Med.* 60, 210–212.
- Yu, X., Wadghiri, Y.Z., Sanez, D.H., Turnbull, D.H., 2005. In vivo auditory brain mapping in mice with Mn-enhanced MRI. *Nat. Neurosci.* 8, 961–968.
- Zhang, X., Bearer, E.L., Boulat, B., Hall, F.S., Uhl, G.R., Jacobs, R.E., 2010. Altered neurocircuitry in the dopamine transporter knockout mouse brain. *PLoS One* 5, e11506.